

Isolated zero mode in a quantum computer from a duality twist

Sutapa Samanta,¹ Derek S. Wang,² Armin Rahmani,^{1,3} and Aditi Mitra⁴

¹*Department of Physics and Astronomy, Western Washington University, Bellingham, Washington 98225, USA*

²*IBM Quantum, IBM T.J. Watson Research Center, Yorktown Heights, New York 10598, USA*

³*Advanced Materials Science and Engineering Center,
Western Washington University, Bellingham, Washington 98225, USA*

⁴*Center for Quantum Phenomena, Department of Physics,
New York University, 726 Broadway, New York, New York 10003, USA*

Investigating the interplay of dualities, generalized symmetries, and topological defects beyond theoretical models is an important challenge in condensed matter physics and quantum materials. A simple model exhibiting this physics is the transverse-field Ising model, which can host a topological defect that performs the Kramers-Wannier duality transformation. When acting on one point in space, this duality defect imposes the duality twisted boundary condition and binds a single zero mode. This zero mode is unusual as it lacks a localized partner in the same Z_2 sector and has an infinite lifetime, even in finite systems. Using Floquet driving of a closed Ising chain with a duality defect, we generate this zero mode in a digital quantum computer. We detect the mode by measuring its associated persistent autocorrelation function using an efficient sampling protocol and a compound strategy for error mitigation. We also show that the zero mode resides at the domain wall between two regions related by a Kramers-Wannier duality transformation. Finally, we highlight the robustness of the isolated zero mode to integrability- and symmetry-breaking perturbations. Our findings provide a method for exploring exotic topological defects, associated with noninvertible generalized symmetries, in digitized quantum devices.

I. INTRODUCTION

Symmetry is a cornerstone of modern physics. Traditionally, symmetries in quantum systems are realized as unitary representations of a group of transformations that leave the Hamiltonian invariant. Dualities are transformations that relate two different models, or different phases of the same model, and are closely related to symmetry but cannot always be described within the traditional framework [1–4]. Duality transformations can act as projectors, which do not admit a unitary representation but are examples of noninvertible symmetries [5–9]. Both unitary (invertible) and noninvertible symmetries are described within the recently developed framework of *generalized symmetries* [10, 11], and can manifest through topological defects [7, 9, 12, 13].

Exploring topological defects, encompassing both invertible and noninvertible types, stands at the forefront of research in condensed matter and high-energy physics [14, 15]. Despite remarkable theoretical progress, detecting exotic topological defects associated with generalized symmetries is challenging in traditional condensed-matter systems, rendering their experimental realization an open question. Here, we realize such a system on a synthetic platform, a small, noisy quantum computer [16].

The Kramers-Wannier duality transformation of the transverse-field Ising model (TFIM) is one of the most well-known dualities [17]. The TFIM can support different topological defects, including the familiar unitary spin-flip defect, which captures the Z_2 symmetry of the model, and the duality defect [7, 9, 18] studied here. The duality defect is one of the simplest examples of a noninvertible transformation as it projects out states of a given Z_2 symmetry [7]. A duality defect acting at a particular point in space imposes a special “twisted” boundary condition [5, 19–25]. One of the consequences of the duality defect is the emergence of a zero mode, bound to the defect, with distinct characteristics from more well-known edge zero modes occurring in the TFIM with open boundary conditions [7, 18].

It is well-established that the TFIM with open boundary conditions can host Majorana zero modes [26, 27] in the topological phase, both in equilibrium and in its Floquet versions [28, 29]. These modes appear in pairs localized at the two edges of the system, and have a lifetime which grows exponentially with the system size because they hybridize leading to an energy splitting that is exponentially small in the system size. On the other hand, the zero mode appearing due to a duality twist defect is isolated, lacking a localized partner in the same Z_2 sector. It thus has an infinite lifetime, even in finite systems. In addition, this isolated mode exists for all couplings of the static and Floquet versions of the TFIM, and separates the chain into two parts whose couplings are related by the Kramers-Wannier duality transformation [7, 30].

Digitized quantum devices have provided a new playground for realizing topological physics [31–38]. In particular, Floquet versions of the TFIM with open boundary conditions have been studied on current noisy quantum devices [37, 39]. In this paper, we probe the Floquet version of the TFIM with a duality twist defect. We implement the duality twist defect in a closed chain of 20 qubits on the `ibmq_kolkata` device and observe signatures of an isolated zero mode. By obtaining the autocorrelation functions of several operators in the quantum device, we demonstrate that the

zero mode, with a theoretically infinite lifetime [18, 30], is persistent. We also confirm that weak perturbations, which break both the integrability and the Z_2 symmetry of the system, do not destabilize the zero mode in finite-length chains.

We further investigate the properties of this mode by applying a local unitary circuit that moves the twist defect. We observe that the zero mode does not follow the defect but remains in its original position. This contrasts sharply with a potential well that binds a localized mode, where moving the potential well would also translate the localized mode. This behavior is a consequence of the fact that the twist defect is topological, meaning that a local unitary transformation can move the defect, while leaving the Hamiltonian invariant when all the couplings are set equal to each other. For unequal couplings, there are still ramifications of the topological properties of the defect, which will be discussed later. Recall that translations do not fall under the category of local unitary transformations, thus this property is not shared by a chain with a local impurity potential.

The paper is organized as follows. In Section II, we introduce the model and define the autocorrelation function utilized for detecting the zero mode. Sections III, IV, and V are focused on results obtained on the IBM quantum computer. In particular, Sec. III discusses the localized zero mode for the integrable model, Sec. IV demonstrates the topological nature of the duality twist and its relation to the Kramers-Wannier duality transformation, Sec. V explores the effects of integrability- and symmetry breaking perturbations, and Sec. VI summarizes our findings. Additional details are provided in three appendices.

II. UNPAIRED ZERO MODE IN THE FLOQUET-TFIM WITH A DUALITY TWIST

We consider the one dimensional TFIM with L sites, whose Hamiltonian is given by $H = J \sum_{j=0}^{L-1} \sigma_j^z \sigma_{j+1}^z + g \sum_{j=0}^{L-1} \sigma_j^x$. The system has no open ends, and periodic boundary conditions are imposed where the operator at site $L+j$ is identified with the operator at site j . Under these periodic boundary conditions and spatially homogeneous couplings, there are no edge modes. One can however make the couplings spatially inhomogeneous, and in particular insert a domain wall that separates a region of $g > J$ from a region of $g < J$. Periodic boundary conditions imply that such domain walls have to appear in pairs. A zero mode resides at each domain wall, leading to a pair of zero modes for periodic boundary conditions. Open boundary conditions also lead to zero modes that appear in pairs at the two edges of the system. The modes can be viewed as Majorana operators, in a fermionic model obtained from a Jordan-Wigner transformation on the spin chain. While local in the fermionic model, these modes are nonlocal in terms of the original spin degrees of freedom. In contrast, it has been shown that duality twisted boundary conditions allow one to introduce an odd number of domain walls in the system [7], and consequently an odd number of zero modes. We discuss this scenario in more detail below.

Duality-twisted boundary conditions, e.g., on the link between sites $r, r-1$, are implemented by changing $\sigma_{r-1}^z \sigma_r^z$ to $\sigma_{r-1}^z \sigma_r^x$, and removing the transverse field $g \sigma_r^x$ [7], while still preserving periodic boundary conditions with operator L identified with operator $L+j$. The duality twisted Hamiltonian then becomes

$$H_t = H_{zz} + H_{zx} + H_x, \quad (1)$$

where

$$H_{zz} = J \sum_{j \neq r-1} \sigma_j^z \sigma_{j+1}^z, \quad H_{zx} = J \sigma_{r-1}^z \sigma_r^x, \quad H_x = g \sum_{j \neq r} \sigma_j^x.$$

Note that with the periodic boundary conditions, in the absence of a twist, the Z_2 symmetry is $\mathcal{D}_\psi = \prod_{j=0}^{L-1} \sigma_j^x$. With the twist, the Z_2 symmetry changes to $\Omega_r = i \sigma_r^z \mathcal{D}_\psi$. A duality twist can also be imposed by considering an infinite chain, and gauging the Z_2 symmetry for one half of the chain [40–45] or by performing a Kramers-Wannier transformation on one half of the chain [46]. One can also derive the above duality twisted Hamiltonian by using techniques from the Ising fusion category [46].

We now perform a Jordan-Wigner (JW) transformation where the JW string starts from the twist, and in particular

from the site that has no transverse field. The $2L$ Majorana fermions are related to the Pauli spins as follows,

$$\gamma_{2(r+j)} = \sigma_{j+r+1}^z \prod_{k=r}^{j+r} \sigma_k^x, \quad j = 0, 1, \dots, L-2, \quad (2a)$$

$$\gamma_{2(r+j)+1} = -\sigma_{j+r+1}^y \prod_{k=r}^{j+r} \sigma_k^x, \quad j = 0, 1, \dots, L-2, \quad (2b)$$

$$\gamma_{2r+2L-2} = \sigma_r^z, \quad \gamma_{2r+2L-1} = -\sigma_r^y, \quad (2c)$$

$$\sigma_{L+j}^\alpha = \sigma_j^\alpha. \quad (2d)$$

Above, the last equation imposes periodic boundary conditions. With the twist, the Z_2 symmetry in terms of the Majorana fermions is

$$\Omega_r = i\sigma_r^z \mathcal{D}_\psi = \gamma_{2r+2L-1} \left[(-i\gamma_{2r}\gamma_{2r+1}) (-i\gamma_{2r+2}\gamma_{2r+3}) \dots (-i\gamma_{2r+2L-4}\gamma_{2r+2L-3}) \right]. \quad (3)$$

Note that Ω_r is a product of $2L-1$ Majorana fermions as it does not contain the $\gamma_{2r+2L-2}$ Majorana fermion. Since it is a string containing odd number of Majorana fermions, we have the following relations

$$\Omega_r \gamma_{2r+2L-2} = -\gamma_{2r+2L-2} \Omega_r, \quad (4)$$

$$\Omega_r \gamma_{2r+2j} = \gamma_{2r+2j} \Omega_r, \quad j = 0 \dots L-2, \quad (5)$$

$$\Omega_r \gamma_{2r+2j+1} = \gamma_{2r+2j+1} \Omega_r, \quad j = 0 \dots L-2. \quad (6)$$

The Hamiltonian H_t in terms of the Majorana fermions becomes

$$H_{zz} = -iJ \sum_{j=0 \dots L-2, j \neq L-1} \gamma_{2(j+r)-1} \gamma_{2(j+r)}, \quad (7)$$

$$H_x = -ig \sum_{j=0 \dots L-2, j \neq L-1} \gamma_{2(r+j)} \gamma_{2(r+j)+1}, \quad (8)$$

$$H_{zx} = -iJ \Omega_r \gamma_{2(r+L)-3} \gamma_{2(r+L)-1}. \quad (9)$$

Even though there are $2L$ Majorana fermions in the Hilbert space, H_t explicitly contains $2L-1$ Majorana fermions as $\gamma_{2(r+L)-2}$ does not enter in H_t . Importantly, although $\gamma_{2r+2L-2}$ does not appear in the Hamiltonian, it is not a zero mode as it does not commute with Ω_r and consequently the Hamiltonian. The string operator appears to make the system interacting, but the problem is still solvable because the $2L-1$ Majorana fermions entering in H_t commute with Ω_r . Thus one may set $\Omega_r = \pm 1$, after which the Hamiltonian is a bilinear in the Majorana fermions. Thus H_t , has eigenmodes obtained by diagonalizing a $(2L-1) \times (2L-1)$ matrix for each Z_2 sector. Since the matrix dimension is odd in each Z_2 sector, this has to yield an odd number of zero modes in each Z_2 sector.

For the parameters above, a given Z_2 sector hosts a zero mode that is localized at r , and has a localization length ξ , where $\exp[1/\xi] \approx \max(g, J)/\min(g, J)$ [18]. There is nothing special about the sites $r, r-1$, and a local unitary transformation can move the twist defect from one pair of sites to the neighboring pair of sites [7, 30, 47] without moving the zero mode [30]. In particular, after a JW transformation this zero mode is a Majorana mode, with the branch-cut or string associated with the zero mode terminating at the duality defect [7]. The local unitary transformation just modifies the length of this branch cut as it does not move the zero mode while moving the site of the duality defect.

Some approaches in the literature (see [48, 49] and appendix of [7]) have also considered a related model that is more physical for fermions, where the string operator is simply dropped to obtain the new model. In this case, there are indeed two zero modes with the second zero mode being $\gamma_{2(r+L)-2}$ which now commutes with the Hamiltonian (as the string operator does not explicitly enter in the Hamiltonian). However, this is a sleight of hand, which is strictly not valid if one is discussing the physics of the original spin chain. In other words, the model with two zero modes where one of them is $\gamma_{2(r+L)-2}$, is a different model. For the spin chain, a proper treatment always leads to the string operator Ω_r , and there is no good reason to drop it. In this case $\gamma_{2(r+L)-2}$ is not a zero mode as it does not commute with H_t due to the string Ω_r .

In summary, the spin chain, has one zero mode in each Z_2 sector, thus when looking at both even and odd Z_2 sectors, $\Omega_r = \pm 1$, there are two zero modes. In what follows, we will perform simulations that do not mix Z_2 sectors. In this case, only a single zero mode will manifest. The above method of solving the problem in each Z_2 sector separately appears in other contexts such as the periodic chain. For this case, the JW transformation to fermions

gives a nonlocal term on one bond where the nonlocal term corresponds to fermion parity that serves as the Z_2 symmetry of the model. Thus, in each symmetry sector, the nonlocal term is replaced by its ± 1 eigenvalue, making the model local.

We now turn to the Floquet version of the above model, which is also the one that will be simulated on the IBM devices. The Floquet unitary operator for the twisted model can be written as [18]

$$U = e^{-iH_x/2} e^{-iH_{xx}/2} e^{-iH_{zz}/2}. \quad (10)$$

As far as symmetries go, much of what was discussed regarding H_t is also valid for U . In particular, in a given Z_2 sector $\Omega_r = \pm 1$, U is exactly solvable as it involves exponentials of fermion bilinears after a JW transformation. In addition, only $2L - 1$ Majorana fermions appear in U , so that we need to diagonalize a $(2L - 1) \times (2L - 1)$ dimensional matrix. Since the orthogonal matrix that evolves the $2L - 1$ Majoranas only performs proper rotations, its determinant has to be 1. This forces an odd number of eigenvalues to be equal to 1, where the corresponding eigenvectors are the zero modes.

The analytic expression for the zero mode for the above Floquet set-up, i.e., with a duality-twist, was derived in [18, 30]. Similar to edge modes with open boundary conditions, the zero mode with a duality twist is a linear superposition of Majoranas all along the chain. For the zero mode with the duality twist, the largest weight in the superposition is with the Majorana in the vicinity of site r . In contrast, the zero mode pairs with open boundary conditions have their largest weight at the boundaries. In addition, one may introduce a single domain wall in the duality-twisted Floquet set-up by making the couplings g, J inhomogeneous [18]. In this case, the zero mode resides at the domain wall. As we shall discuss further, a series of local unitary transformations can relate the homogeneous Floquet unitary of (10) to one where a single domain wall is present [30].

The Majorana zero mode with a duality twist has important differences with the Majorana pairs that appear for open boundary conditions. While the latter occurs only in the topological phase $J > g$, the Majorana zero mode with the duality twist occurs for all values of g, J , including $g > J, g < J$ and even disordered ones. Only its localization length is determined by the strength of the disorder and average values of g and J . Since the zero mode with the duality twist lacks a partner, it never decays in time, i.e., it has an infinite lifetime rather than a lifetime that is exponentially large in the system size. The mathematical reason for this is that the zero mode with the duality twist is a symmetry of the system as it commutes both with the generator of time evolution U , as well as the Z_2 symmetry Ω_r . In contrast, the Majorana pairs with open boundary conditions anticommute with the associated Z_2 symmetry. We emphasize that a single zero mode in a given Z_2 sector for the duality twisted model follows from a simple counting argument as summarized above.

In the spin representation, the zero mode at site r has an overlap with the Pauli operator σ_r^y [18, 30]. (In the figures, we denote $\sigma_i^{x,y,z}$ with X_i, Y_i, Z_i for notational brevity.) In addition, the farther away a Majorana is from the duality twist at r , the longer is the corresponding Pauli string (this is because, in order to make the model have only local terms, the JW transformation has to start from the twist). To detect the Majorana zero mode, we employ the infinite temperature autocorrelation function, defined as

$$A_{\mathcal{O}}(n) = \frac{1}{2^L} \text{Tr} \left[\mathcal{O}(n) \mathcal{O} \right], \quad (11)$$

of an operator \mathcal{O} , where the Heisenberg operator after n Floquet steps is given by $\mathcal{O}(n) = (U^\dagger)^n \mathcal{O} U^n$. The signature of the zero mode is the temporal persistence of a nonzero autocorrelation function for σ_r^y . In contrast, the autocorrelation function of other operators, with no overlap with a conserved quantity, are expected to decay to zero due to dephasing.

To measure the autocorrelation function, we represent the trace as a sum of expectation values $\langle k | \mathcal{O}(n) \mathcal{O} | k \rangle$ in a basis chosen to be the eigenbasis of \mathcal{O} , $\mathcal{O} | k \rangle = \lambda_k | k \rangle$. Each expectation value in the trace can then be measured by measuring $\langle \mathcal{O}(n) \rangle$ at time n after applying the Floquet circuit to the initial state $| k \rangle$. For operators \mathcal{O} corresponding to Pauli operators (or Pauli strings), the states $| k \rangle$ can be chosen to be easy-to-prepare direct products of single-qubit states. The detection of the trace can nevertheless seem challenging because we have an exponentially large number of basis states $| k \rangle$. However, a random sampling of a small number of basis states and performing a partial sum yield accurate approximations to the trace (11), as discussed in Appendix A.

III. DETECTION OF THE UNPAIRED ZERO MODE IN THE IBM QUANTUM DEVICE

We have chosen the values of the coupling constants to be $J = 0.75\pi$ and $g = 0.2\pi$ for all the computations in this paper, although similar results can be obtained for other coupling constants. To create and detect the zero mode in the quantum computer, we apply a quantum circuit that generates the Floquet dynamics by the repeated applications of a circuit block corresponding to the unitary operator in (10). A simple 4-qubit version of this block, corresponding

through rotation operators $R_y(\pi/2)$ ($R_x(-\pi/2)$) that rotate from the z to the x (y) direction.

In Fig. 2, we present both noiseless simulation and noisy quantum-hardware results for the bulk and defect autocorrelation functions obtained from the partial trace with 20 random basis states. We also show noiseless simulation results from Qiskit Aer simulators for 12-qubit and 20-qubit systems. The simulation results exhibit very small system-size dependence, indicating that the 20-qubit system accurately captures the thermodynamic limit. Furthermore, the results from the `ibmq_kolkata` device for the 20-qubit system is in good agreement with the noiseless simulations. We observe that the autocorrelation function of $\mathcal{O} = \sigma_r^y$ at the twist defect $r = L - 1$ does not decay, which overlaps with the emergent Majorana zero mode. In contrast, all other autocorrelators decay to zero in the long time limit. The persistence of the autocorrelation function of the operator corresponding to the unpaired zero mode, during the Floquet dynamics, provides evidence for the dynamical generation of this mode in a digitized quantum device.

IV. UNITARY TRANSLATION OF TWIST DEFECT

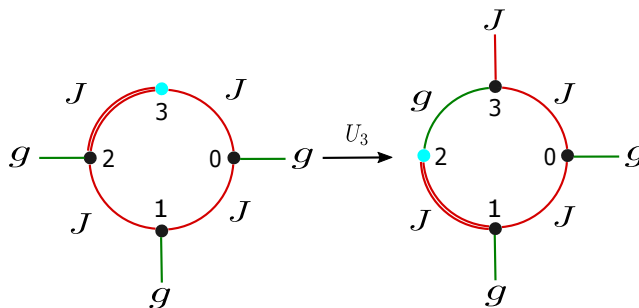


FIG. 3. A twist defect that was originally on sites 2 and 3 (left) is moved to sites 1 and 2 (right) by a unitary transformation $CZ_{2,3}H_2$. Cyan denotes the site r at which there is no magnetic field while the double red lines denote a twist interaction $\sigma_{r-1}^z \sigma_r^x$. Vertical lines denote a transverse field while solid lines between sites $j, j+1$ denote a $\sigma_j^z \sigma_{j+1}^z$ interaction. After the unitary transformation (right), note the Kramers-Wannier duality between sites 2,3 and the rest of the chain where the strength of the transverse field at site 3 is J while the exchange interaction between qubits 2 and 3 is g . The unitary transformation shifts the twist but not the Majorana zero mode which stays localized at site 3. Thus the Majorana zero mode resides at the domain wall across which g, J exchange roles.

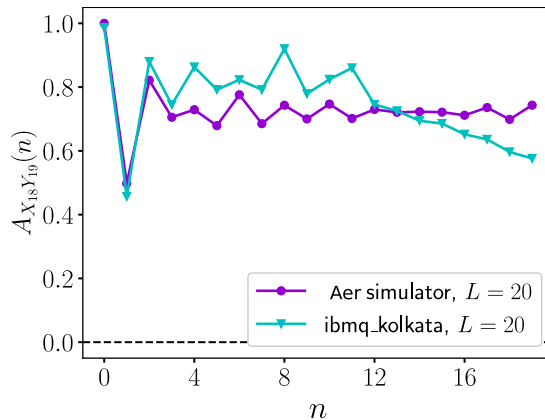


FIG. 4. Unpaired Majorana in the `ibmq_kolkata` device for $L = 20$ after a unitary translation that has moved the twist defect from sites 18,19 to sites 17,18. The Majorana stays localized at site 19 but now has an overlap with the longer Pauli string $\sigma_{18}^x \sigma_{19}^y$. Date of demonstration is 5th May, 2023.

A hallmark of a topological defect is that it can be moved by local unitary transformations, while leaving the model invariant. Strictly speaking the model is invariant only for $g = J$, and in the high frequency limit. Nevertheless, even away from this special case, physical consequences of the topological nature of this defect manifest in the invariance of the position of the zero mode as the twist defect is moved.

A local unitary transformation of the form $U_r = CZ_{r-1,r}H_{r-1}$, where $CZ_{r-1,r}$ is a controlled-Z gate, and H_{r-1} is a Hadamard gate, moves the twist-defect from the sites $(r-1, r)$ to sites $(r-2, r-1)$ [7, 30]. Fig. 3 illustrates

this for a 4-qubit system. The unitary U_r introduces a transverse field at site r of strength J while eliminating the transverse field at site $r - 1$. It also changes the terms $J\sigma_{r-2}^z\sigma_{r-1}^z$ and $J\sigma_{r-1}^z\sigma_r^x$ to $J\sigma_{r-2}^z\sigma_{r-1}^x$ and $g\sigma_{r-1}^z\sigma_r^z$. Thus a Kramers-Wannier duality transformation has been performed on the sites $r, r - 1$ where the roles of g, J have been interchanged. Remarkably, the Majorana zero mode stays localized at r , and now separates two regions of the chain that are related by the Kramers-Wannier duality transformation. Although the Majorana zero mode stays localized at site r , in the language of Pauli strings, it is a more nonlocal object. In particular, instead of having an overlap with σ_r^y , it now has an overlap with $\sigma_{r-1}^x\sigma_r^y$.

The Majorana zero mode after a translation of the twist defect from (18, 19) to (17, 18) for a 20-qubit system is shown in Fig. 4. After one translation, the Majorana is still localized at site $r = 19$, but in the language of Pauli spins, this Majorana zero mode no longer has an overlap with σ_{19}^y , but rather with the longer string $\sigma_{18}^x\sigma_{19}^y$.

V. EFFECTS OF INTERACTIONS

Now we add perturbations to the model (1) through the term

$$H_{xx} = J_x \sum_j \sigma_j^x \sigma_{j+1}^x. \quad (12)$$

In the language of Majorana fermions, the above is a four-fermion and hence interacting term. The Floquet unitary is now given by

$$U_{\text{int}} = e^{-iH_{xx}/2} e^{-iH_x/2} e^{-iH_{zx}/2} e^{-iH_{zz}/2}. \quad (13)$$

Note that H_{xx} not only breaks integrability, but it also does not commute with the discrete symmetry Ω_r due to the $\sigma_{r\pm 1}^x\sigma_r^x$ terms. We repeat the same quantum simulation for the interacting model with the defect location at site $r = L - 1$. We find that the σ_r^y -correlator at the defect remains constant, while all other correlators decay with time as shown in Fig. 5. We observe a similar behavior to the noninteracting case shown in Fig. 2 for both bulk and defect autocorrelation functions, within the studied number of Floquet cycles.

We note, however, that the long time dynamics of the σ_r^y -correlator at the defect is not captured in this figure as we can run the Floquet dynamics in the device only for about 20 Floquet cycles before noise takes over. We show the theoretical behavior of the Majorana zero mode by performing exact diagonalization for long times in Fig. 6(a). After the initial decay to the first plateau, the Majorana mode decays to a second plateau. The plateau heights decrease with increasing interactions J_x . We capture only the initial portions of this behavior in the quantum device [see Fig. 6(b) and (c)], i.e the decay to the first plateau. While the first plateau height is not L dependent (as seen in the simulations in Fig. 5), we expect that the second plateau height is L dependent, where as $L \rightarrow \infty$, the plateau height decreases to zero. This is because, there is no exact zero mode when we break integrability, with the zero mode decaying via scattering with bulk excitations [51]. However, a finite size system blocks these scattering processes leading to a partial decay, and hence a plateau height which is inversely related to system size [30]. A second important observation is that while the interactions now couple the two Z_2 sectors, yet the zero modes in the two sectors do not efficiently couple to each other as is evident by the appearance of the second plateau, which persists at long times. This is again a finite system size effect.

VI. CONCLUSIONS

In this paper, we investigated the physics of the duality twist defect and the corresponding emergent zero mode in a periodically driven TFIM loop of 20 qubits on the IBM superconducting quantum device. The interplay of topological effects and symmetries can lead to novel phenomena. The zero mode generated by a duality twist in a TFIM chain commutes with the Z_2 charge of the model and thus, theoretically, has an infinite lifetime in finite systems [18] (in contrast to edge states with open boundary conditions that are vulnerable to exponential hybridization). Using efficient random sampling, we obtained an accurate approximation to various autocorrelation functions and provided evidence, on the quantum computer, for the emergence of the unpaired zero mode bound to the duality twist defect. Furthermore, we explored the effects of moving the duality twist defect with unitary gates, and the effect of integrability- and symmetry-breaking perturbations. This work opens a new avenue for physically creating and investigating topological defects in quantum systems, and exploring their ramifications on nonequilibrium dynamics, a topic poorly understood theoretically.

Future improvements in hardware quality and error mitigation may allow accessing longer evolution times with deeper circuits, providing access to the long-time plateaus of persistent autocorrelation functions in the presence of

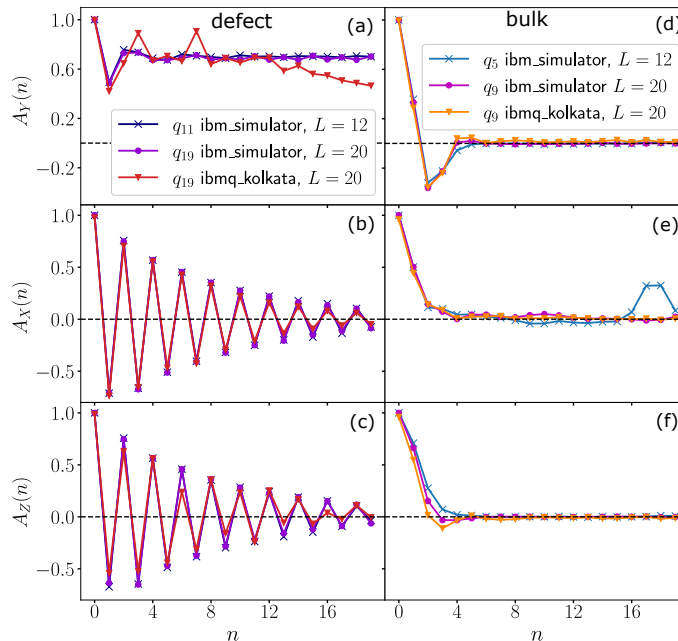


FIG. 5. Signature of the Majorana zero mode at the defect site for duality-twisted interacting Floquet-TFIM. Panel (a) shows the nondecaying autocorrelation for σ_y at the defect site $r = L - 1$, which overlaps with the zero mode. All other autocorrelations both at the twist defect $r = L - 1$ [panel (b), (c)] and at a bulk site $j = -1 + L/2$ [panel (d), (e), (f)], far away from the twist defect, decay with time. The chosen bulk qubit behaves qualitatively similarly to other bulk qubits. We present data from `ibmq_kolkata` device for $L = 20$, the longest physical loop of qubits available in the device. There is good qualitative agreement between noiseless simulations and measurements on the noisy quantum device. The noiseless simulations were also performed for a smaller system of 12 qubits. The agreement between the two system sizes $L = 12, 20$ indicates that we capture the behavior in the thermodynamic limit for these times. At longer times, we expect a stronger L dependence discussed in the main text. The label q_i indicates measurement of the i th qubit. Date of demonstrations is 22nd April, 2023.

interactions. Exciting directions of future research include implementing topological defects on the quantum computer, not only in Z_n spin chains [9], but also in two-dimensional Floquet codes [52].

ACKNOWLEDGMENTS

We thank Oles Shtanko for helpful comments and discussions. We acknowledge the use of IBM Quantum services. We also thank the Brookhaven National Laboratory for providing access to IBM devices. This work was supported by the US National Science Foundation under Grants NSF DMR-2018358 (AM) and DMR-1945395 (AR and SS), and in part by the US National Science Foundation under Grant No. NSF PHY-1748958 (AR and AM).

Appendix A: Convergence of the partial trace

In this section, we provide evidence for the accurate approximation of the autocorrelation functions (based on the full trace) by a partial trace with a small number of random basis states. In Fig. 7, we show the expectation value with a single random state, and the partial trace with 20 random initial states, and we compare them with the full trace calculated with all 2^{12} basis states for a system of size $L = 12$. We have calculated these quantities for all three Pauli operators. Even a single expectation value is relatively close to the exact (full trace) autocorrelation function, for both bulk and defect sites, due to the little variation between these expectation values. The results of the partial trace with 20 random states are in excellent agreement with the full trace, supporting the use of the partial trace to approximate the autocorrelation functions.

All expectation values are the same, and correspond to the Y autocorrelation function at the defect site. Thus for this particular observable, the trace is independent of the number of basis states used.

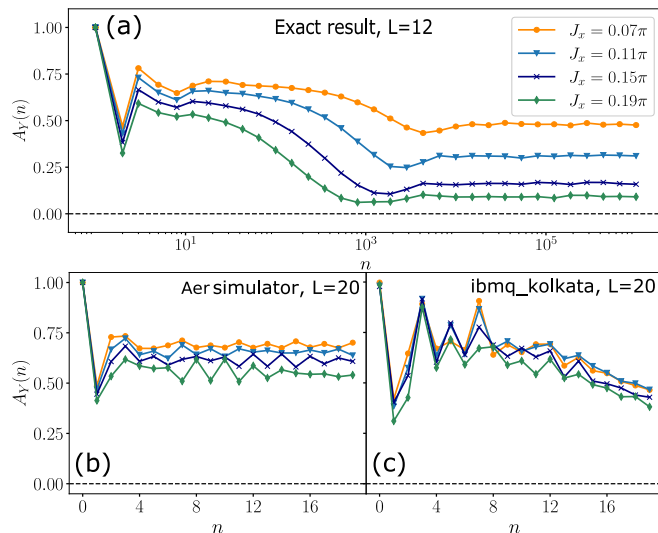


FIG. 6. Stability of the Majorana zero mode to integrability- and symmetry-breaking perturbations in a finite system. The autocorrelation function of σ_r^y at the defect $r = L - 1$, for different values of the perturbation J_x , are presented. Panel (a) shows the numerical results for system size $L = 12$ up to large Floquet time steps. After the initial transient corresponding to the appearance of a first plateau, the autocorrelation stabilizes at a second plateau. This is a finite size effect where the height of the second plateau vanishes as $L \rightarrow \infty$ [30]. While we are not able to access this second plateau in the long-time limit in the `ibmq_kolkata` device due to noise, panels (b) and (c) show results from the IBM simulator and the `ibmq_kolkata` device, respectively, for intermediate timescales. At these timescales, the formation of the first plateau is clearly visible. Date of demonstrations is 27th April, 2023.

Appendix B: Error Mitigation

We employ a composite error mitigation strategy combining error suppression and mitigation techniques [53]. Noisy bitstrings resulting from each shot are first mitigated by correcting readout errors using the method of Ref. 54, which utilizes calibration circuits scaling linearly with the number of qubits. Finally, zero-noise extrapolation is applied by extrapolating measured probabilities to the zero-noise value [55, 56]. This is achieved by performing measurements with 8,000 shots at noise factors of 1 (applying the original circuit) and 3 (evolving the system forward by the original circuit, backward by appending the inverse of the original circuit, and finally forward again by reapplying the original circuit [57]). A line through 1 and 3 on the horizontal axis yield the zero-noise extrapolated value at the intercept with the vertical axis.

Appendix C: Layout of the computing device and its characteristics

The layout of `ibmq_kolkata` device is shown in Fig. 8. We use the 20 qubit loop consisting of qubits 1, 2, 3, 5, 8, 11, 14, 16, 19, 22, 25, 24, 23, 21, 18, 15, 12, 10, 7, and 4 for our demonstrations. We choose the link between qubit 12 and qubit 15 to place the twist defect. The readout length for all these runs was $640ns$. P_{01} (P_{10}) is the probability that measuring a qubit gives 0 (1) immediately after preparing it in state 1 (0). The readout error is indicated as RE, and the frequency f and the anharmonicity a are both in GHz. The calibration data from 18th April, 2023 for the used qubits are given in Table I, and the error map is shown in Fig. 9. The calibration data from 22nd April, 2023 for the used qubits are given in Table II, and the error map is shown in Fig. 10. The calibration data from 27th April, 2023 for the used qubits are given in Table III, and the error map is shown in Fig. 11. The calibration data from 5th May, 2023 for the used qubits are given in Table IV, and the error map is shown in Fig. 12. The error maps are generated using Qiskit's visualization library.

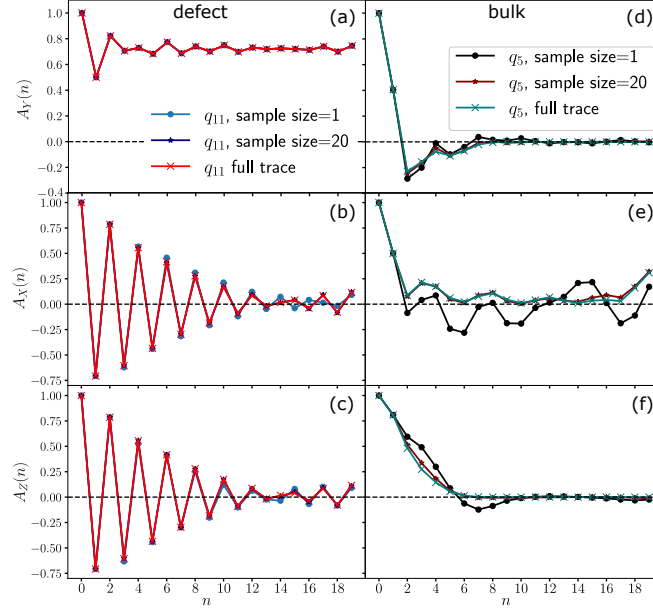


FIG. 7. Autocorrelation functions from computing the partial trace in a classical computer for different sample sizes of random initial states, for system size $L = 12$. The left panels [panel (a), (b), (c)] show the autocorrelation functions at the site of twist defect $r = L - 1$, while the right panels [panel (d), (e), (f)] are for a site far away from it, $j = -1 + L/2$.

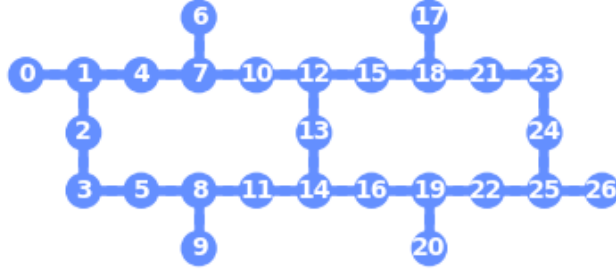


FIG. 8. Qubit layout of `ibmq_kolkata` device

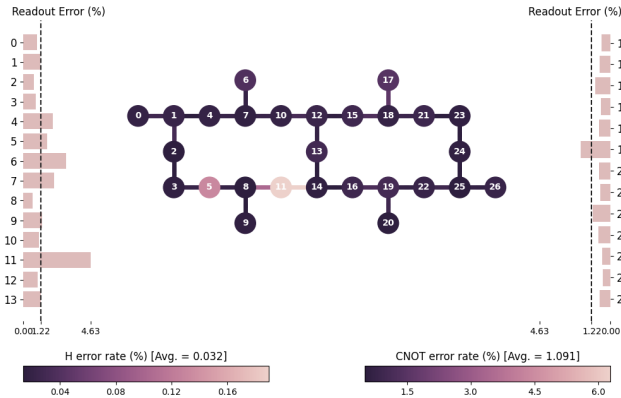


FIG. 9. Error map for qubits and couplings of `ibmq_kolkata` device from 18th April, 2023.

Qubit	T1(μ s)	T2(μ s)	f	a	RE	P_{01}	P_{10}
1	81.37	181.74	4.99	-0.34	0.0087	0.0112	0.0062
2	72.9	52.5	5.11	-0.34	0.0155	0.022	0.009
3	126.2	165.5	4.87	-0.35	0.013	0.0122	0.0138
5	128.1	29.5	5.11	-0.342	0.0325	0.0344	0.0306
8	135.2	60.4	4.93	-0.345	0.0427	0.0292	0.0562
11	132.8	43.6	4.87	-0.373	0.1247	0.1182	0.1312
14	58.82	70.08	5.12	-0.343	0.06	0.0216	0.0984
16	78.78	116.12	5.22	-0.34	0.0092	0.0078	0.0106
19	86.69	32.28	5.002	-0.345	0.0383	0.0208	0.0558
22	108.02	39.49	5.127	-0.343	0.0369	0.0352	0.0386
25	253.27	83.23	4.92	-0.347	0.0098	0.0124	0.0072
24	120.36	86.38	5.004	-0.346	0.0092	0.0096	0.0088
23	153.89	48.45	5.138	-0.343	0.0135	0.0214	0.0056
21	83.88	17.18	5.274	-0.341	0.0073	0.0108	0.0038
18	163.04	104.59	5.097	-0.344	0.0102	0.0126	0.0078
15	175.32	207.31	5.041	-0.344	0.0053	0.007	0.0036
12	148.89	137.72	4.96	-0.346	0.0088	0.01	0.0076
10	113.57	44.2	5.178	-0.342	0.0151	0.014	0.0162
7	164.47	33.13	5.031	-0.346	0.0223	0.0208	0.0238
4	87.74	87.38	5.224	-0.341	0.0214	0.0224	0.0204

TABLE I. Calibration data for the qubits used for demonstrations on 18th April, 2023.

Qubit	T1(μ s)	T2(μ s)	f	a	RE	P_{01}	P_{10}
1	17.686	106.2	4.99	-0.345	0.0203	0.0272	0.0134
2	42.29	37.02	5.117	-0.343	0.0516	0.078	0.0252
3	143.82	188.71	4.866	-0.346	0.0102	0.0114	0.009
5	103.63	30.41	5.113	-0.342	0.032	0.0332	0.0308
8	163.56	50.83	4.928	-0.345	0.0451	0.032	0.0582
11	139.18	39.37	4.868	-0.373	0.1176	0.1116	0.1236
14	128.15	67.17	5.117	-0.343	0.0629	0.0246	0.1012
16	96.47	92.36	5.222	-0.34	0.0111	0.0084	0.0138
19	112.28	26.24	5.002	-0.345	0.0776	0.0316	0.1236
22	115.85	38.87	5.127	-0.343	0.0411	0.0383	0.0438
25	167.11	81.57	4.92	-0.347	0.0088	0.0122	0.0054
24	122.28	83.58	5.004	-0.346	0.0083	0.0108	0.0058
23	127.04	42.31	5.138	-0.343	0.0143	0.026	0.0026
21	69.81	16.35	5.274	-0.341	0.0069	0.0078	0.006
18	70.17	105.99	5.097	-0.344	0.0087	0.0086	0.0088
15	157.17	192.35	5.041	-0.344	0.0061	0.008	0.0042
12	144.32	174.84	4.961	-0.346	0.0075	0.0092	0.0058
10	88.61	35.82	5.178	-0.342	0.0106	0.0144	0.0068
7	68.69	34.22	5.031	-0.345	0.0242	0.0254	0.023
4	108.36	66.99	5.224	-0.341	0.0216	0.0202	0.023

TABLE II. Calibration data for the qubits used for demonstrations on 22nd April, 2023.

Qubit	T1(μ s)	T2(μ s)	f	a	RE	P_{01}	P_{10}
1	249.53	176.45	4.991	-0.345	0.0112	0.012	0.0098
2	10.43	44.90	5.117	-0.343	0.0149	0.019	0.0108
3	75.96	136.94	4.866	-0.346	0.0143	0.0158	0.0128
5	133.18	31.47	5.113	-0.342	0.0323	0.0324	0.0322
8	125.48	49.20	4.928	-0.345	0.0342	0.0328	0.0356
11	149.91	41.34	4.868	-0.373	0.0944	0.0956	0.0932
14	165.77	204.37	5.117	-0.343	0.0657	0.0244	0.107
16	106.17	84.22	5.222	-0.34	0.009	0.007	0.011
19	54.53	23.02	5.002	-0.345	0.0387	0.0252	0.0522
22	138.54	34.42	5.127	-0.343	0.0372	0.037	0.0374
25	222.14	120.88	4.921	-0.347	0.0109	0.0156	0.0062
24	93.44	106.77	5.005	-0.346	0.0094	0.0104	0.0084
23	135.32	52.53	5.138	-0.343	0.0035	0.005	0.002
21	124.1	18.48	5.274	-0.341	0.0047	0.0052	0.0042
18	117.51	148.1	5.097	-0.344	0.0094	0.0112	0.0076
15	129.05	224.34	5.041	-0.344	0.0067	0.0072	0.0064
12	205.67	225.1	4.961	-0.346	0.0075	0.0084	0.0066
10	85.16	38.17	5.178	-0.342	0.0087	0.0094	0.008
7	170.34	45.36	5.031	-0.346	0.0261	0.0202	0.032
4	122.95	100.49	5.224	-0.341	0.0196	0.021	0.0182

TABLE III. Calibration data for the qubits used for demonstrations on 27th April, 2023.

Qubit	T1(μ s)	T2(μ s)	f	a	RE	P_{01}	P_{10}
1	176.13	214.04	4.991	-0.345	0.0099	0.0146	0.0052
2	10.9	44.9	5.113	-0.343	0.0149	0.019	0.0108
3	96.79	195.85	4.866	-0.346	0.0128	0.0118	0.0138
5	88.86	29.91	5.113	-0.342	0.0348	0.0348	0.0348
8	129.58	52.25	4.928	-0.345	0.0277	0.0248	0.0306
11	133.31	37.53	4.868	-0.373	0.123	0.1296	0.1164
14	156.54	169.92	5.117	-0.343	0.066	0.022	0.11
16	113.15	103.99	5.222	-0.3402	0.0079	0.008	0.0078
19	105.14	28.67	5.002	-0.345	0.0699	0.025	0.1148
22	116.19	32.82	5.127	-0.343	0.0382	0.0344	0.042
25	194.42	73.42	4.921	-0.347	0.0056	0.0072	0.004
24	107.53	107.29	5.005	-0.346	0.0097	0.0106	0.0088
23	115.88	50.13	5.138	-0.343	0.0044	0.0058	0.003
21	94.18	19.34	5.274	-0.341	0.0062	0.0062	0.0062
18	145.87	125.4	5.097	-0.344	0.0092	0.0104	0.008
15	91.18	153.23	5.041	-0.344	0.0066	0.0084	0.0048
12	175.97	188.79	4.961	-0.346	0.0078	0.009	0.0066
10	120.79	38.97	5.178	-0.342	0.015	0.0092	0.0208
7	144.69	54.6	5.031	-0.346	0.0239	0.0292	0.0186
4	145.79	139.71	5.225	-0.341	0.0232	0.0248	0.0216

TABLE IV. Calibration data for the qubits used for demonstrations on 5th May, 2023.

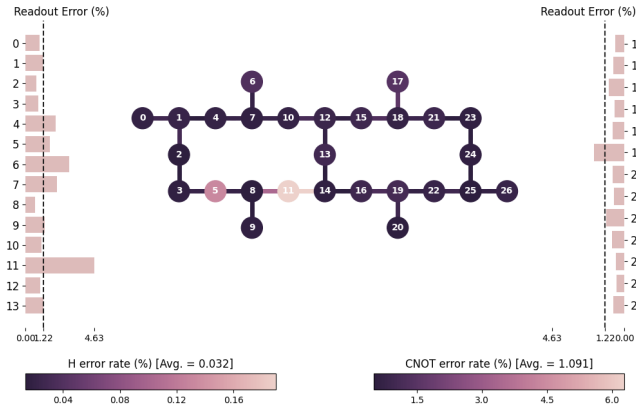


FIG. 10. Error map for qubits and couplings of `imbq_kolkata` device from 22nd April, 2023

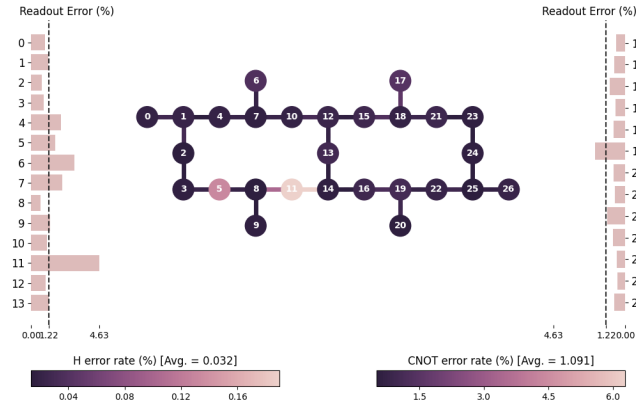


FIG. 11. Error map for qubits and couplings of `imbq_kolkata` device from 27th April, 2023

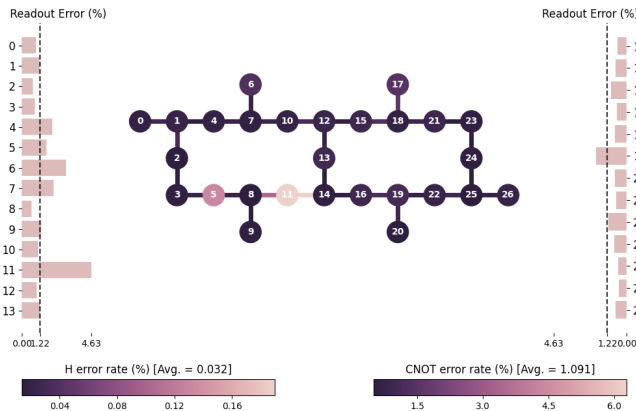


FIG. 12. Error map for qubits and couplings of `imbq_kolkata` device from 5th May, 2023

-
- [1] E. Cobanera, G. Ortiz, and Z. Nussinov, The bond-algebraic approach to dualities, *Adv. Phys.* **60**, 679 (2011).
- [2] N. Seiberg, T. Senthil, C. Wang, and E. Witten, A duality web in 2+1 dimensions and condensed matter physics, *Ann. Phys.* **374**, 395 (2016).
- [3] A. M. Somoza, P. Serna, and A. Nahum, Self-dual criticality in three-dimensional z_2 gauge theory with matter, *Phys. Rev. X* **11**, 041008 (2021).
- [4] L. Lootens, C. Delcamp, G. Ortiz, and F. Verstraete, Dualities in one-dimensional quantum lattice models: symmetric hamiltonians and matrix product operator intertwiners, arXiv:2112.09091 (2021).
- [5] E. Verlinde, Fusion rules and modular transformations in 2d conformal field theory, *Nucl. Phys. B* **300**, 360 (1988).
- [6] L. Bhardwaj, L. E. Bottini, S. Schäfer-Nameki, and A. Tiwari, Non-invertible higher-categorical symmetries, *SciPost Phys.* **14**, 007 (2023).
- [7] D. Aasen, R. S. K. Mong, and P. Fendley, Topological defects on the lattice: I. the ising model, *J. Phys. A: Math. Theor.* **49**, 354001 (2016).
- [8] R. Thorngren and Y. Wang, Fusion category symmetry i: Anomaly in-flow and gapped phases, arXiv:1912.02817 (2019).
- [9] D. Aasen, P. Fendley, and R. S. Mong, Topological defects on the lattice: dualities and degeneracies, arXiv:2008.08598 (2020).
- [10] L. Kong, T. Lan, X.-G. Wen, Z.-H. Zhang, and H. Zheng, Algebraic higher symmetry and categorical symmetry: A holographic and entanglement view of symmetry, *Phys. Rev. Res.* **2**, 043086 (2020).
- [11] J. McGreevy, Generalized Symmetries in Condensed Matter, arXiv:2204.03045 (2022).
- [12] D. Gaiotto, A. Kapustin, N. Seiberg, and B. Willett, Generalized global symmetries, *J. High Energy Phys.* **2015** (2), 172.
- [13] D. Gaiotto, J. H. Lee, and J. Wu, Integrable kondo problems, *J. High Energy Phys.* **2021** (4).
- [14] M. Cheng and N. Seiberg, Lieb-schultz-mattis, luttinger, and 't hooft – anomaly matching in lattice systems, arXiv:2211.12543 (2023).
- [15] L. Eck and P. Fendley, From the xxz chain to the integrable rydberg-blockade ladder via non-invertible duality defects, arXiv:2302.14081 (2023).
- [16] J. Preskill, Quantum Computing in the NISQ era and beyond, *Quantum* **2**, 79 (2018).
- [17] H. A. Kramers and G. H. Wannier, Statistics of the two-dimensional ferromagnet. Part 1., *Phys. Rev.* **60**, 252 (1941).
- [18] M. T. Tan, Y. Wang, and A. Mitra, Topological defects in floquet circuits, *SciPost* **16**, 075 (2024).
- [19] J. L. Cardy, Boundary conditions, fusion rules and the verlinde formula, *Nucl. Phys. B* **324**, 581 (1989).
- [20] G. Schutz, 'duality twisted' boundary conditions in n-state potts models, *Journal of Physics A: Mathematical and General* **26**, 4555 (1993).
- [21] M. Oshikawa and I. Affleck, Boundary conformal field theory approach to the critical two-dimensional ising model with a defect line, *Nuclear Physics B* **495**, 533 (1997).
- [22] V. B. Petkova and J. B. Zuber, Generalized twisted partition functions, *Phys. Lett. B* **504**, 157 (2001).
- [23] U. Grimm, Spectrum of a duality twisted Ising quantum chain, *J. Phys. A* **35**, L25 (2002), arXiv:hep-th/0111157.
- [24] J. Fröhlich, J. Fuchs, I. Runkel, and C. Schweigert, Kramers-wannier duality from conformal defects, *Phys. Rev. Lett.* **93**, 070601 (2004).
- [25] C.-M. Chang, Y.-H. Lin, S.-H. Shao, Y. Wang, and X. Yin, Topological defect lines and renormalization group flows in two dimensions, *J. High Energy Phys.* **01**, 026.
- [26] A. Y. Kitaev, Unpaired majorana fermions in quantum wires, *Phys.-Usp.* **44** (2001).
- [27] P. Fendley, Strong zero modes and eigenstate phase transitions in the xyz/interacting majorana chain, *Journal of Physics A: Mathematical and Theoretical* **49**, 30LT01 (2016).
- [28] M. Thakurathi, A. A. Patel, D. Sen, and A. Dutta, Floquet generation of majorana end modes and topological invariants, *Phys. Rev. B* **88**, 155133 (2013).
- [29] D. J. Yates, F. H. L. Essler, and A. Mitra, Almost strong $(0, \pi)$ edge modes in clean interacting one-dimensional floquet systems, *Phys. Rev. B* **99**, 205419 (2019).
- [30] A. Mitra, H.-C. Yeh, F. Yan, and A. Rosch, Nonintegrable floquet ising model with duality twisted boundary conditions, *Phys. Rev. B* **107**, 245416 (2023).
- [31] A. Rahmani, K. J. Sung, H. Putterman, P. Roushan, P. Ghaemi, and Z. Jiang, Creating and manipulating a laughlin-type $\nu = 1/3$ fractional quantum hall state on a quantum computer with linear depth circuits, *PRX Quantum* **1**, 020309 (2020).
- [32] K. Satzinger et al, Realizing topologically ordered states on a quantum processor, *Science* **374**, 1237 (2021).
- [33] J. P. T. Stenger, N. T. Bronn, D. J. Egger, and D. Pekker, Simulating the dynamics of braiding of majorana zero modes using an ibm quantum computer, *Phys. Rev. Res.* **3**, 033171 (2021).
- [34] Y.-J. Liu, K. Shtengel, A. Smith, and F. Pollmann, Methods for simulating string-net states and anyons on a digital quantum computer, *PRX Quantum* **3**, 040315 (2022).
- [35] A. Kirmani, K. Bull, C.-Y. Hou, V. Saravanan, S. M. Saeed, Z. Papić, A. Rahmani, and P. Ghaemi, Probing geometric excitations of fractional quantum hall states on quantum computers, *Phys. Rev. Lett.* **129**, 056801 (2022).
- [36] T. I. Andersen et al, Non-abelian braiding of graph vertices in a superconducting processor, *Nature* **618**, 264 (2023).
- [37] N. Harle, O. Shtanko, and R. Movassagh, Observing and braiding topological majorana modes on programmable quantum simulators, *Nat. Comm.* **14**, 2286 (2023).
- [38] A. Kirmani, D. S. Wang, P. Ghaemi, and A. Rahmani, Braiding fractional quantum hall quasiholes on a superconducting quantum processor, arXiv:2303.04806 (2023).

- [39] X. Mi and et al, Noise-resilient edge modes on a chain of superconducting qubits, *Science* **378**, 785 (2022).
- [40] M. Sinha, F. Yan, L. Grans-Samuelsson, A. Roy, and H. Saleur, Lattice realizations of topological defects in the critical (1+1)-d three-state Potts model, *JHEP* **07**, 225, arXiv:2310.19703 [hep-th].
- [41] N. Seiberg, S. Seifnashri, and S.-H. Shao, Non-invertible symmetries and LSM-type constraints on a tensor product Hilbert space, *SciPost Phys.* **16**, 154 (2024), arXiv:2401.12281 [cond-mat.str-el].
- [42] A. Parayil Mana, Y. Li, H. Sukeo, and T.-C. Wei, Kennedy-Tasaki transformation and noninvertible symmetry in lattice models beyond one dimension, *Phys. Rev. B* **109**, 245129 (2024), arXiv:2402.09520 [cond-mat.str-el].
- [43] A. Chatterjee, Ömer M. Aksoy, and X.-G. Wen, Quantum phases and transitions in spin chains with non-invertible symmetries, *SciPost Phys.* **17**, 115 (2024).
- [44] D.-C. Lu, Z. Sun, and Y.-Z. You, Realizing triality and p -ality by lattice twisted gauging in (1+1)d quantum spin systems, arxiv.2405.14939 (2024).
- [45] W. Cao, L. Li, and M. Yamazaki, Generating lattice non-invertible symmetries, *SciPost Phys.* **17**, 104 (2024).
- [46] F. Yan, R. Konik, and A. Mitra, Duality defect in a deformed transverse-field ising model, arXiv:2410.17317 (2024).
- [47] M. Hauru, G. Evenbly, W. W. Ho, D. Gaiotto, and G. Vidal, Topological conformal defects with tensor networks, *Phys. Rev. B* **94**, 115125 (2016).
- [48] D. Rogerson, F. Pollmann, and A. Roy, Entanglement entropy and negativity in the ising model with defects, *Journal of High Energy Physics* **2022**, 10.1007/jhep06(2022)165 (2022).
- [49] A. Roy and H. Saleur, Entanglement entropy in the ising model with topological defects, *Phys. Rev. Lett.* **128**, 090603 (2022).
- [50] O. Shtanko, D. S. Wang, H. Zhang, N. Harle, A. Seif, R. Movassagh, and Z. Mineev, Uncovering local integrability in quantum many-body dynamics, arXiv:2307.07552 (2023).
- [51] H.-C. Yeh, A. Rosch, and A. Mitra, Decay rates of almost strong modes in floquet spin chains beyond fermi's golden rule, *Phys. Rev. B* **108**, 075112 (2023).
- [52] M. B. Hastings and J. Haah, Dynamically Generated Logical Qubits, *Quantum* **5**, 564 (2021).
- [53] K. J. Ferris, A. J. Rasmusson, N. T. Bronn, and O. Lanes, Quantum Simulation on Noisy Superconducting Quantum Computers, arXiv:2209.02795[quant-ph] (2022).
- [54] P. D. Nation, H. Kang, N. Sundaresan, and J. M. Gambetta, Scalable mitigation of measurement errors on quantum computers, *PRX Quantum* **2**, 040326 (2021).
- [55] Y. Li and S. C. Benjamin, Efficient variational quantum simulator incorporating active error minimization, *Phys. Rev. X* **7**, 021050 (2017).
- [56] K. Temme, S. Bravyi, and J. M. Gambetta, Error mitigation for short-depth quantum circuits, *Phys. Rev. Lett.* **119**, 180509 (2017).
- [57] P. Rivero, F. Metz, A. Hasan, A. M. Brańczyk, and C. Johnson, Zero noise extrapolation prototype, <https://github.com/qiskit-community/prototype-zne> (2022).